The Seismic Record
A journal of the Seismological Society of America

Seismic Node Arrays for Enhanced Understanding and Monitoring of Geothermal Systems

Thomas Samuel Hudson[*1,2], Tom Kettley[1], John-Michael Kendall[1], Tom O'Toole[3], Andrew Jupe[4], Robin K. Shail[5], and Augusta Grand[6]

Abstract

Harnessing geothermal energy will likely play a critical role in reducing global CO_2 emissions. However, exploration, development, and monitoring of geothermal systems remain challenging. Here, we explore how recent low-cost seismic node instrumentation advances might enhance geothermal exploration and monitoring. We show the results from 450 nodes deployed at a geothermal prospect in Cornwall, United Kingdom. First, we demonstrate how the nodes can be used to monitor the spatiotemporal and size distribution of induced seismicity. Second, we use focal mechanisms, shear-wave source polarities, and anisotropy to indicate how the dense passive seismic observations might provide enhanced insight into the stress state of the geothermal systems. All the methods are fully automated, essential for processing the data from many receivers. In our example case study, we find that the injection-site fracture orientations significantly differ from that of the crust above and the regional stress state. These observations agree well with fracture orientations inferred from independent well-log data, exemplifying how the nodes can provide new insight for understanding the geothermal systems. Finally, we discuss the limitations of nodes and the role they might play in hybrid seismic monitoring going forward. Overall, our results emphasize the important role that low-cost, easy-to-deploy dense nodal arrays can play in geothermal exploration and operation.

Cite this article as Hudson, T. S., T. Kettley, J.-M. Kendall, T. O'Toole, A. Jupe, R. K. Shail, and A. Grand (2024). Seismic Node Arrays for Enhanced Understanding and Monitoring of Geothermal Systems, *The Seismic Record*. **4**(**3**), 161–171, doi: 10.1785/0320240019.

Supplemental Material

Introduction

Geothermal systems provide an energy resource with minimal CO_2 emissions. Exploiting the geothermal resources will likely become increasingly important as society transitions to a CO_2-neutral future. However, the exploration, development, and subsequent operation of these subsurface fluid resources can be complex and expensive. Mapping the presence of fluids and fractures is important for informing the operators of where the geothermal fluids migrate and accumulate, derisking exploration by identifying optimal drill sites. During development and operation, fluids migrating along the faults can reduce fault-normal stresses, potentially triggering induced seismicity (Baria *et al.*, 1989; Zang *et al.*, 2014; Edwards *et al.*, 2015; Sherburn *et al.*, 2015, Holmgren and Werner, 2021). Monitoring and locating any induced seismicity is important for mitigating seismic hazard, mapping fluid migration, and understanding the subsurface response to injection or extraction (e.g., Igonin *et al.*, 2021; Kettley *et al.*, 2021). Seismology can also quantify stress state, especially fracture orientation (e.g., Arnold and Townend, 2007; Zhang *et al.*, 2019), and map faults and fluids spatially (Napolitano *et al.*, 2020; Gauntlett *et al.*, 2023; Hudson, Kendall, *et al.*, 2023), further derisking drilling and operation of geothermal assets.

1. Department of Earth Sciences, University of Oxford, Oxford, United Kingdom, https://orcid.org/0000-0003-2944-883X (TSH); https://orcid.org/0000-0002-4412-5265 (TK); https://orcid.org/0000-0002-1486-3945 (J-MK); 2. Department of Earth Sciences, ETH Zürich, Zürich, Switzerland; 3. STRYDE Ltd, London, United Kingdom, https://orcid.org/0009-0000-9327-3179 (TO); 4. Altcom Ltd, Penzance, United Kingdom; 5. Camborne School of Mines, University of Exeter, Cornwall, United Kingdom, https://orcid.org/0000-0001-7200-5124 (RKS); 6. Eden Geothermal Ltd, Cornwall, United Kingdom, https://orcid.org/0000-0002-5982-4026 (AG)

*Corresponding author: thomas.hudson@erdw.ethz.ch

Recent developments in seismic instrumentation allow for sampling the seismic wavefield with an order of magnitude more receivers than previously possible. Distributed acoustic sensing (DAS) (Lellouch *et al.*, 2020) allows in-axis strain to be measured along optical fibers at meter resolution. Similarly, low-cost seismic nodes now enable 100s–1000s of receivers to be deployed in networks or arrays (Parker *et al.*, 2018; Obermann *et al.*, 2022; Ourabah and Chatenay, 2022). Here, we investigate how automated processing of dense nodal datasets can be used for microseismic monitoring and provide enhanced insight into the injection site and shallower crustal fracture orientations, at the Eden Geothermal site, Cornwall, United Kingdom. Finally, we explore the benefits and limitations of seismic nodes, including a brief outlook on the future of seismic instrumentation at geothermal prospects.

Methods

Experiment details

450 STRYDE nodes were deployed at the Eden Geothermal deep geothermal project in Cornwall, United Kingdom, from November to December 2022 (see Fig. 1). STRYDE nodes are low-cost, fast-to-deploy, single-component instruments (~$100/channel, deployment time <30 s), using piezoelectric technology to measure acceleration with a flat instrument response from 1 to 125 Hz and a sensitivity of 3.6 V/g (see the supplemental material, available to this article, for full instrument response and example noise spectra). In this experiment, we not only deployed single nodes vertically but also in a three-component configuration at some locations (see Fig. 1 for respective locations and supplemental material for an example site). Three-component deployment is possible due to the nature of the piezoelectric sensor, which can record data in arbitrary orientations, in contrast to traditional mass-movement devices (Ourabah *et al.*, 2021). We also deployed multiple nodes in the same orientation at some locations to investigate data stacking performance. All data are sampled at 500 Hz. Ten conventional broadband seismometers were also deployed with a similar network aperture during the experiment (see Fig. 1).

Microseismic detection and location

Microseismicity is detected using the back-migration method QuakeMigrate (Hudson *et al.*, 2019). This searches for a coalescence of energy from multiple receivers in both space and time. A particular benefit is that this method is sensitive to coherent earthquake signals close to the noise level, minimizing false triggers caused by incoherent noise, with performance scaling with several receivers. Seismicity is then relocated using NonLinLoc (Lomax and Virieux, 2000). The velocity model used throughout is the British Geological Survey Southwest England 1D layered model (Booth, 2010). Detection and location parameters, as well as the velocity model, are given in the supplemental material. Although the velocity model is regional, we deem it valid for this study because most receivers are within 10s meters of bedrock and we obtain earthquake depths consistent within 100 m of the injection site. 3D body-wave velocity tomography would be poorly constrained by the spatial distribution of seismicity, and no active seismic survey data are available.

Quantifying fracture orientations

In this study, we infer the subsurface fracture orientation both within the injection-site region (from shear-wave source polarizations and focal mechanisms) and in the crust above (from anisotropy).

We infer the dominant fracture or crystallographic orientation of the crust above the injection site using shear-wave velocity anisotropy. For a single dominant anisotropic fabric, two parameters describe this anisotropy: ϕ, the angle of the fast direction with respect to north; and δt, the delay time between fast and slow shear-wave arrivals. This anisotropy can be caused by multiple mechanisms, such as crystallographic-preferred orientation and shape-preferred orientation anisotropy (Kendall, 2000; Savage *et al.*, 2016). Regardless of the mechanism, the orientation of anisotropy is a proxy for the historic or current stress state of the medium. Because of the large number of receivers, we use the fully automated shear-wave splitting analysis method, SWSPy (Hudson, Asplet, and Walker, 2023). We filter the results by removing measurements with uncertainty: $\alpha_{\phi} > 10^{0}$; $\alpha_{\delta t} > 0.1$ s; and a factor representing the quality of the measurement, $Q_W < 0.5$ (Wuestefeld *et al.*, 2010). We also randomly check the individual measurements to confirm the quality of the results. The examples of good and poor splitting measurements are shown in the supplemental material.

Injection-site fault orientations are measured in two ways: *S*-wave source polarization and focal mechanisms. For an earthquake source with a shear-failure component, the *S*-wave source polarization corresponds to the direction of fault slip, even if the earthquake source is not entirely double couple (DC). However, the bulk medium is anisotropic, so we measure the *S*-wave polarization only on waveforms with shear-wave splitting effects

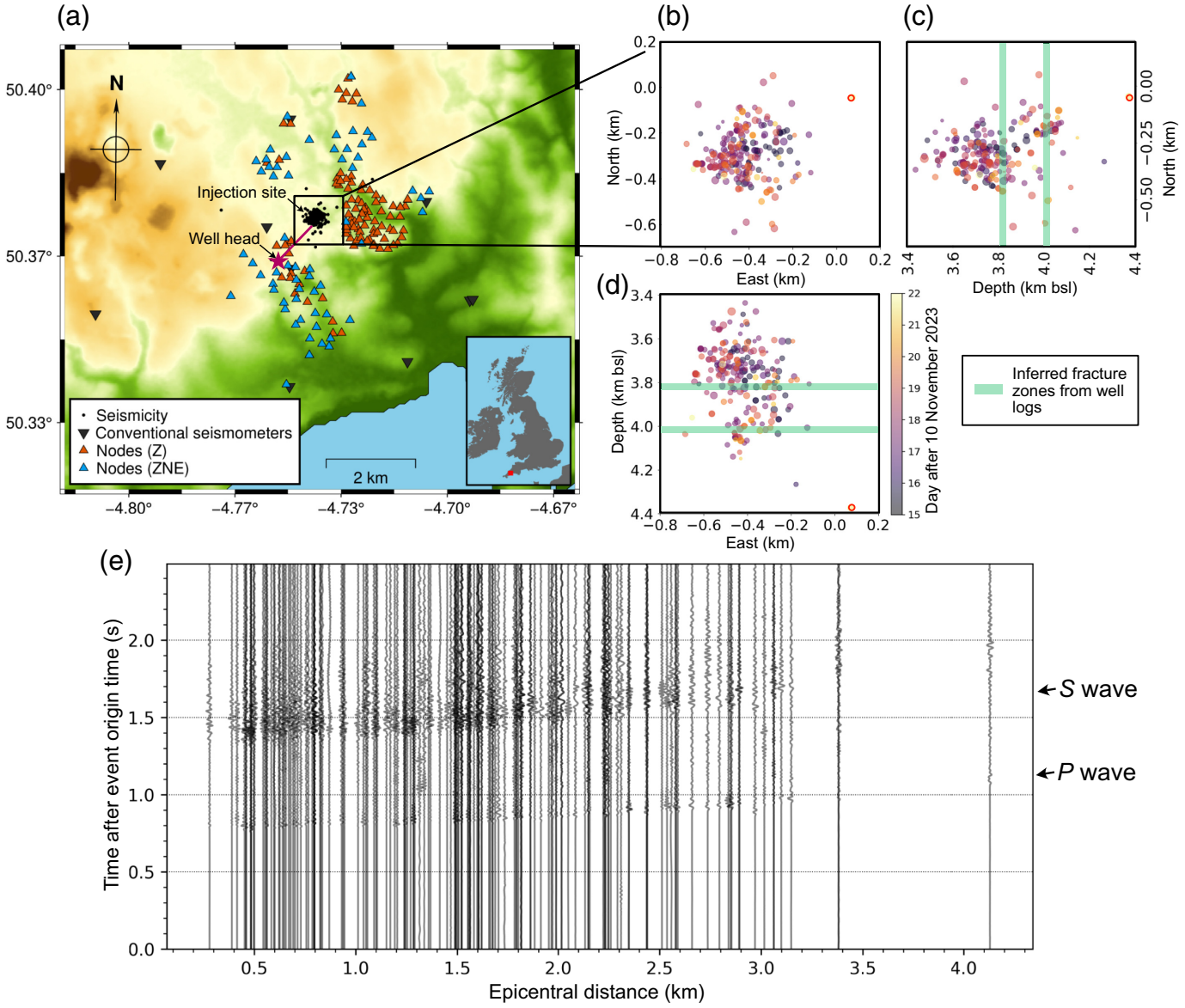

approximately removed (particle motions linearized and time-shifted), which have passed the aforementioned quality checks. The focal mechanism inversion procedure is also automated due to data volumes (248 earthquakes at 450 receivers). Because we only have a 1D estimate of crustal velocity structure, we perform a *P*-wave polarity source inversion rather than a full-waveform inversion, using the Bayesian MTFit algorithm (Pugh and White, 2018). The *P*-wave polarities are measured automatically using the method of Pugh *et al.* (2016). Although earthquakes studied here could have nonzero volumetric components, we force our inversions to be DC constrained because our network geometry would limit the constraint of higher-parameter non-DC solutions in any case.

Figure 1. Relocated earthquake catalog. (a) Map view of the overall experiment. Nodes are shown by orange (vertical component) and blue (three-component) triangles. The black inverted triangles are a network of semipermanent conventional seismometers (not used in this study). Topography is Shuttle Radar Topography Mission (SRTM) data. Seismicity is shown by dense cluster of black dots near the injection well. Well head is shown by pink star (labeled) and well by pink line. (b–d) Detailed map of seismicity, colored by time. (e) Record section for the largest earthquake on the vertical component (a smaller earthquake example is included in the supplemental material).

Earthquake size

The seismic moment release of an earthquake, M_0, combined with the corner frequency, f_c, of the earthquake spectrum can

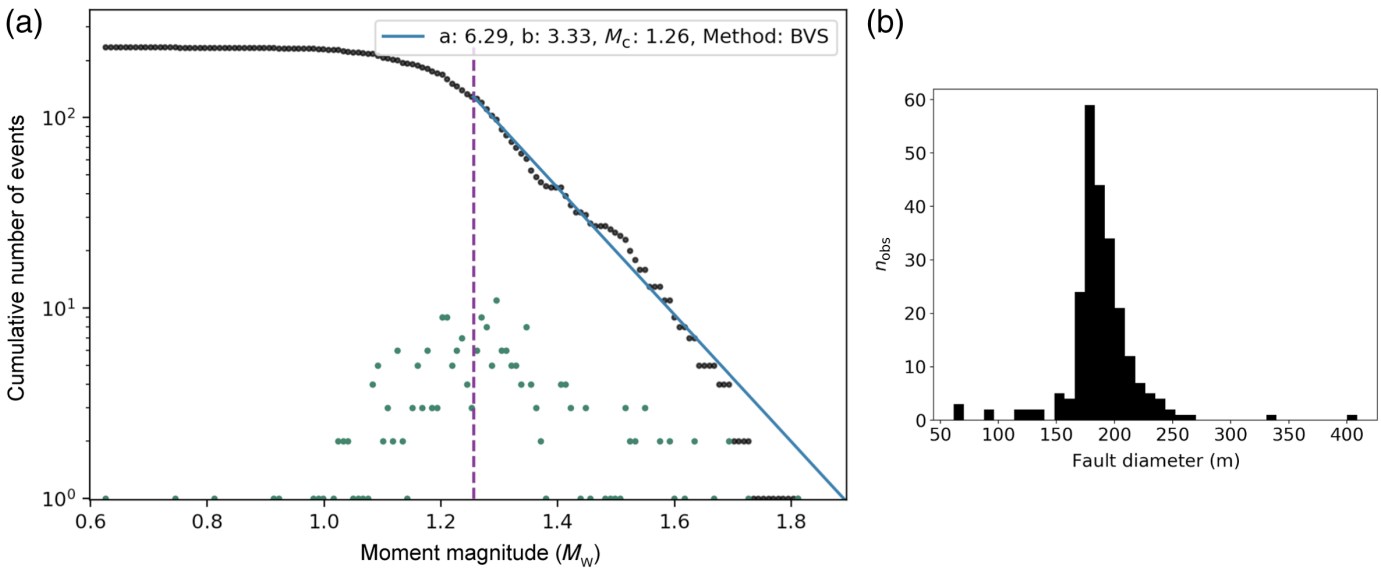

Figure 2. Earthquake catalog moment, fault size, and attenuation distribution. (a) Gutenberg–Richter distribution of moment magnitudes (M_w). (b) Histogram of fault diameters calculated from spectral ratio analysis.

provide information on the size and extent of an earthquake (Madariaga, 1976). Seismic moments are calculated by fitting a Brune model to the displacement spectra (Brune, 1970) using a spectral-ratio method to isolate source and path effects, especially attenuation (see Hudson, Kendall, *et al.*, 2023 and references therein). Displacement is obtained by integrating the node time series twice in the time domain and correcting for the instrument response accordingly (see the supplemental material for instrument response).

Results

The earthquake catalog is shown in Figure 1. We detect 248 earthquakes, most located within 500 m of the injection site (~4 km bsl), clustered in depth near two inferred fracture zones from well-log estimates of where fluids enter the formation. Any finer-scale clustering is hidden by the spatial uncertainty (average horizontal and vertical uncertainties are of the order of 100 m). Spatiotemporal trends are therefore challenging to discern. Although the deployment was for 25 days, we only plot earthquakes from 25 November to 2 December, since more than 95% of events occur over this period postfluid injection.

Figure 2a shows the earthquake moment magnitude distribution. The magnitude of completeness of the catalog is ~1.3. The *b*-value is elevated (>1), as expected for fluids reducing fault-normal stresses, with a particularly high value likely resulting from the use of M_w rather than M_L (Hudson *et al.*, 2022) and/or because earthquakes are induced. Fault diameters are calculated to be typically 150–250 m (Fig. 2b).

Focal mechanisms for a subset of seismicity are shown in Figure 3a. We only include events where we have some confidence of both the automated polarity measurements and fault-plane constraint. The dominant mechanism is thrust faulting. There is also a trend in fault orientation across events, with source mechanisms reversing polarities depending upon whether the earthquake is north or south of the cluster centroid. Furthermore, between the southerly and northerly clusters, the focal mechanisms appear to capture a rotation in the vertical nodal plane, elucidating a transition between southerly and northerly behavior. Figure 3b,c shows the results for one event in detail. Although the vertical nodal plane is somewhat poorly constrained azimuthally (±25° for the event in Fig. 3b), the fault dips and hence the overall 180° rotation in the mechanism are well constrained. Figure 3c confirms the performance of the automated *P*-wave polarity method for a selection of receivers distributed across the focal sphere. The arrivals are clearly impulsive, with automated phase arrival-time picks generally identifying the first motion correctly. The automated polarity measurements are all correct, even for the receivers with higher uncertainty arrival times.

Figure 4 shows the horizontal orientation of fault structures inferred from seismic observations at the injection site and in the crust above, indicating how the passive seismic observations from nodes can be used to shed light on crustal fracture

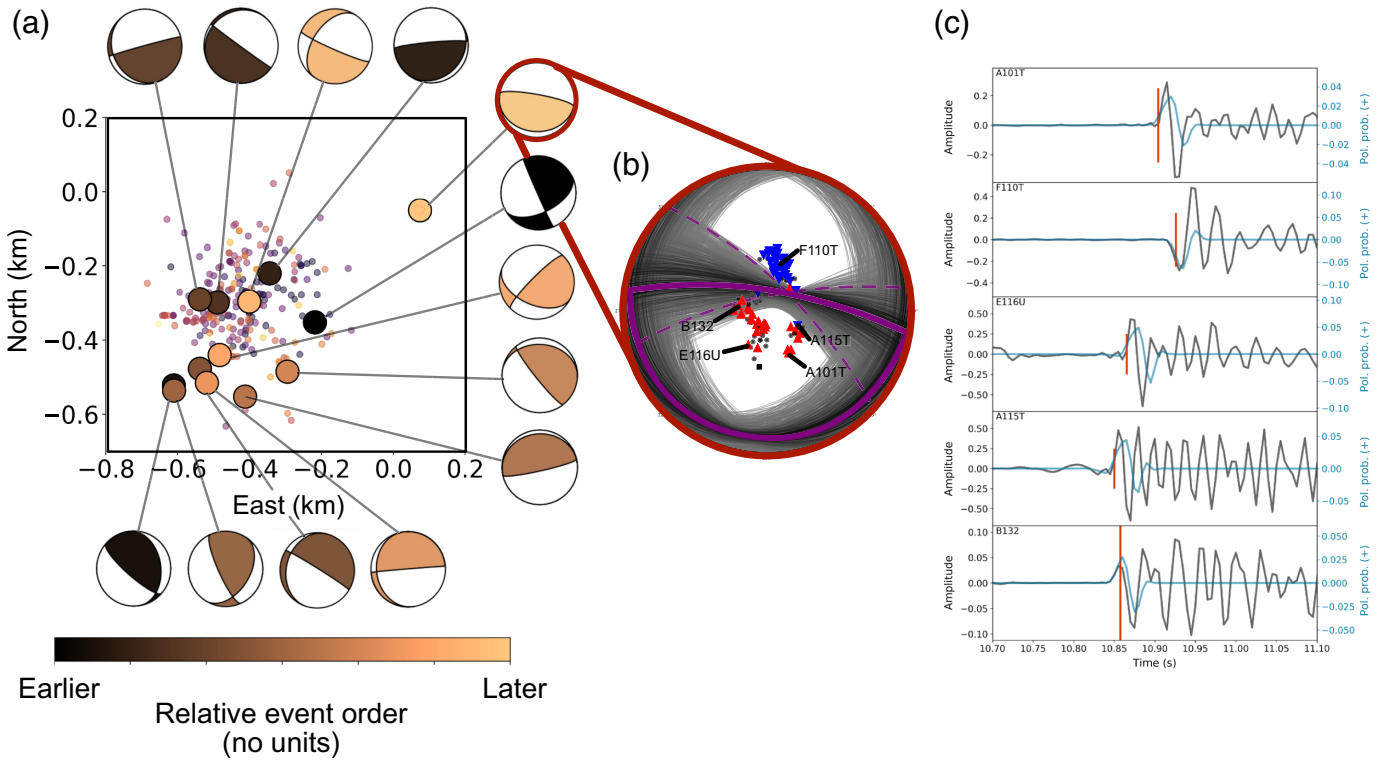

Figure 3. Focal mechanism solutions. (a) Map plot of double-couple (DC)-constrained focal mechanisms for which a solution could be found. All projections are lower hemisphere. Moment tensor inversions are constrained from *P*-wave polarity alone, measured using the automated algorithm described in the Methods section. Events are colored for identification purposes only. (b) The best-constrained event in more detail. The red points are receivers with compressional first arrivals, the blue points are dilatational first arrivals, and the black points are undefined. The black lines indicate 1% highest-likelihood fault-plane solutions from Monte Carlo sampling (representative of variation in focal mechanism orientation), with the best-fitting solution shown by the purple lines (estimated uncertainty indicated by purple dashed lines). (c) Examples of some of the phase arrivals for the receivers are labeled in panel (b). Waveforms are shown in black, and polarity probability is in blue. The red lines correspond to automatically derived *P*-wave first breaks from QuakeMigrate. Further detailed focal mechanism solutions for some of the other events in panel (a) can be found in the supplemental material.

orientations. Horizontal information only is plotted because the anisotropy measurements are assumed to be sensitive to azimuthal variations only. Focal mechanisms and *S*-wave source polarizations provide insight into the in situ fracture orientation within the fluid injection region. *S*-wave source polarizations indicate that the horizontal component of the fault slips dominantly trends north–south, with focal mechanism vertical nodal planes expected to be perpendicular to this. This is the case for the example event focal mechanism nodal plane azimuth (green dashed line, Fig. 4, from the focal mechanism in Fig. 3b), which is representative of the general focal mechanism trend in Figure 3a. Orientations of fractures and/or crystal structure above the injection region are inferred from *S*-wave velocity anisotropy, with the fast *S*-wave directions striking approximately north-northeast–south-southwest. We assume *S*-wave ray paths arrive at vertical incidence (all energy polarized in the horizontal plane). This is likely valid for the crustal velocity structure in Cornwall. We only interpret the dominant *S*-wave anisotropy signal in Figure 4. The orientations perpendicular to the dominant *S*-wave anisotropy signal could be real or the result of cycle-skipping, which we have attempted to remove. The dominant *S*-wave velocity anisotropy fast directions could be caused by microfractures or a preferred crystal orientation, with *S*-wave fast directions oriented parallel to either feature.

In either case, fast *S*-wave direction is inferred to represent either the present-day or paleo-dominant crustal stress orientation above the fluid injection region. If the anisotropy is somewhat controlled by fractures, then there is an apparent discrepancy between fracture orientations within the injection region and shallower fracture orientations. This could be due to a present-day difference in the stress state at different depths or more likely that fractures at the injection site are somewhat

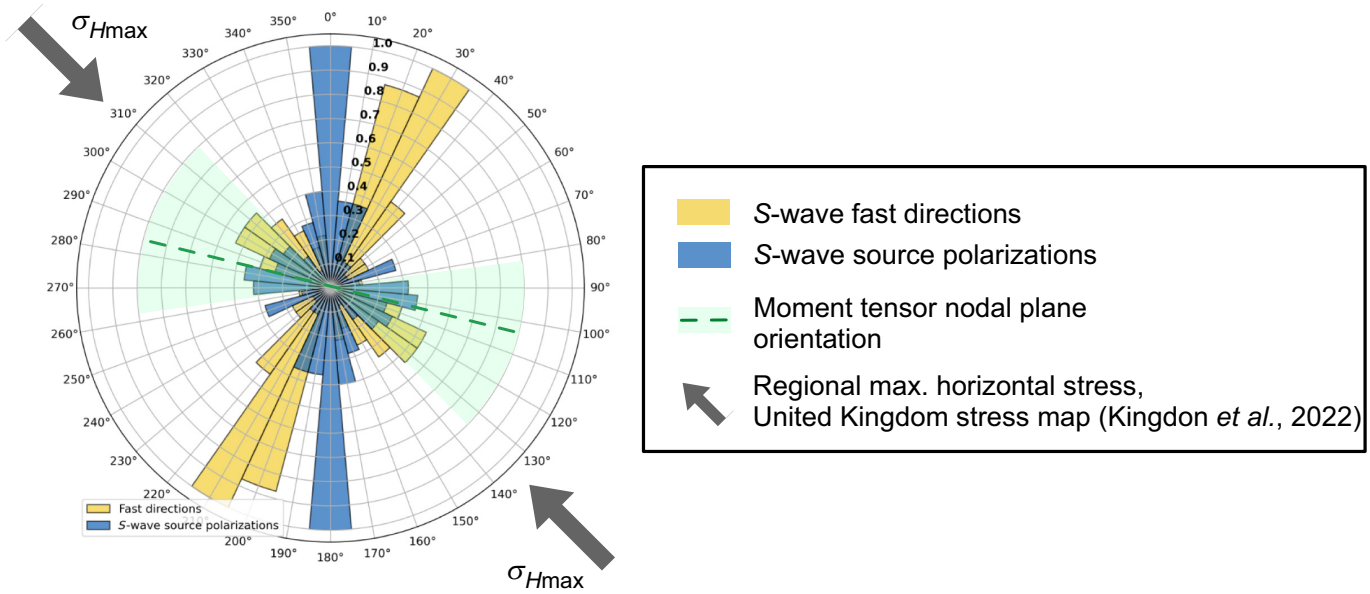

controlled by the current stress field and the *S*-wave anisotropy measurements represent fractures formed in a previous regional paleostress regime. Regional $\sigma_{H\,\max}$ data further complicate interpretation, inconsistent with focal mechanisms at the injection site or the anisotropy-inferred stress orientation at shallower depths.

Figure 4. Horizontal fracture orientations from this study compared to regional expected σ_H. Rose histogram of azimuthal fault-slip directions (*S*-wave source polarizations), fast *S*-wave directions, moment tensor vertical nodal plane azimuthal orientation for the representative example event in Figure 3b and regional stress orientation from the United Kingdom stress map data (Kingdon *et al.*, 2022).

Discussion and Conclusions

Monitoring induced seismicity

Any injection or extraction of subsurface fluids inevitably poses a risk of triggering induced seismicity (Grigoli *et al.*, 2017). Monitoring induced seismicity is essential for assessing changes in subsurface stress state and hence seismic hazard. Quantifying the size distribution of earthquakes is important for attempting to predict the maximum potential size of induced seismicity and hence mitigate triggering such an earthquake (Goertz-Allmann and Wiemer, 2012; Clarke *et al.*, 2019). It is therefore important to detect as many events as possible. Increasing the number of receivers theoretically increases the detection sensitivity of a network by $\sqrt{n}$.

However, seismic node technology is nascent, with nodes currently not as sensitive to ground motion as conventional seismometers. Furthermore, nodes are deployed at the surface rather than downhole or in vaults, so are not isolated from wind and other surface noise. Although individual nodes are less sensitive with a higher self-noise than conventional seismometers, we detect ~15% more events using 450 nodes (248 microearthquakes) compared to the financially more costly network of 10 seismometers (214 microearthquakes). Assuming that more small earthquakes are triggered than we can detect, one might expect the node network to perform better than this, especially given the enhanced spatial sampling. We attribute the only small detection increase partly due to the lower sensitivity of the nodes compared to the seismometers and partly due to the likely high noise levels at the study site due to the proximity to anthropogenic noise and the Atlantic Ocean (see Fig. 1). Although noise levels are high at the study site, we expect this to be the case for many geothermal systems, which are typically located close to populated areas. Nonetheless, the node-derived catalog still increases the number of events detected.

The enhanced spatial coverage of the wavefield provided by the nodes also reduces hypocentral uncertainty, particularly in depth. Here, we find that we can locate seismicity 4 km below the surface to within tens to hundreds of meters of well-log-imaged fracture zones (see Fig. 1). Theoretically, this uncertainty would be further reduced if more nodes were deployed. We attempted to refine hypocenters further using the relative relocation techniques (Trugman and Shearer, 2017), but are

not confident that hypocenters are improved, perhaps because the local velocity structure is approximately homogeneous within the fracture region (which is of the order of our seismic wavelengths), or it is so heterogeneous that it cannot be adequately constrained. We cannot resolve any migration in seismicity with time, but more nodes would further reduce hypocentral uncertainty, allowing one to clearly identify any spatial–temporal trends.

Although the nodes show promise for monitoring induced seismicity, especially regarding cost and ease-of-deployment, their fundamental drawbacks are: (1) battery-life limited deployment time (one month for STRYDE nodes); and (2) a lack of real-time telemetry. We therefore recommend that nodes be used in combination with conventional seismometers to provide enhanced monitoring during stimulation, with conventional instrumentation providing long-term monitoring.

Elucidating subsurface fracture orientations

The nodes show promise for elucidating subsurface fractures. The increased density and spatial extent of observations help constrain both the vertical orientation of moment tensor inversions (Fig. 3) and provide sufficient independent observations to identify dominant trends in the shear-wave source polarization and shear-wave velocity anisotropy data (Fig. 4). Figure 5 summarizes the seismically inferred local fracture orientations within the injection region and at shallower depth compared to independent measurements of fracture orientation from borehole logs.

In the injection region, focal mechanisms indicate subvertical, dominantly thrust faulting, with opposing azimuthal strikes to the north and south of the seismicity centroid. We interpret these faults to most likely slip on the subvertical nodal plane because σ_v would likely lock any horizontal faults. Although focal mechanism strikes are not well constrained, the reversal of compressional quadrants is. Between these two distinct groups of earthquakes, focal mechanism strikes rotate, exhibiting somewhat of a strike-slip behavior. The fault-enclosed region descends relative to the surrounding medium. Shear-wave source polarities indicate that the horizontal components of these subvertical faults slip dominantly north–south. This agrees closely with the dominant orientation of open/partially open fractures from independently measured acoustic borehole imagery (ABI) data from the Eden Geothermal EG-1 well (Fig. 5e). These observations suggest that regional σ_H does not represent the injection region σ_H (nearest regional σ_H measurements from 50 km to the southwest, Kingdon *et al.*, 2022). This is likely explained by local perturbations to the stress field during stimulation (Schoenball *et al.*, 2014), although one should note that focal mechanisms do not necessarily align with the local stress orientation if failure occurs on pre-existing fractures (McKenzie, 1969).

Above the injection region, shear-wave velocity anisotropy analysis indicates that *S*-wave fast directions trend dominantly north-northeast–south-southwest (Fig. 5a). These are parallel to the dominant fracture set orientations from formation microresistivity imaging well logs (Fig. 5b). Drilling-induced tensile fractures and breakouts in the upper 2500 m of the EG-1 well (deviation from vertical <10°) indicate that the local σ_H is overwhelmingly orientated northwest–southeast (mean azimuth 134°). Collectively, these data indicate that the dominant north-northeast–south-southwest *S*-wave fast direction is controlled by fractures and/or compositional banding with similar north-northeast–south-southwest strike rather than the orientation of maximum horizontal stress, σ_H.

In summary, fracture orientations from the nodal dataset closely agree with borehole log observations both at the injection site and in the shallower crust. Our findings demonstrate the added value that a dense nodal array can provide: In this example, showing that regional inferred stress orientations (σ_H) cannot be assumed to represent the injection site stress regime, such information is important for planning future stimulation operations and mitigating seismic hazard.

Because STRYDE nodes have not previously been used for passive seismology on these scales, we conservatively compensated for lower node sensitivity by deploying the network within a 5 km aperture. However, because the nodes detect every earthquake also detected by the seismometer network, we would deploy a wider aperture network in the future. This would increase the coverage of the focal sphere, leading to better-constrained moment tensor solutions. It would also enhance the potential for passive seismic imaging.

Future outlook

The cost per channel and compact design of nodes facilitate the deployment of hundreds/thousands of receivers at lower cost and logistical effort than tens of seismometers. Although the nodes deployed are single component, we show that they can be deployed effectively in a three-component arrangement. Here, we provide an example of how high-density spatial sampling can enhance our understanding of geothermal systems. Specifically, more receivers allow one to detect more earthquakes, provide sufficient hypocentral constraint to link

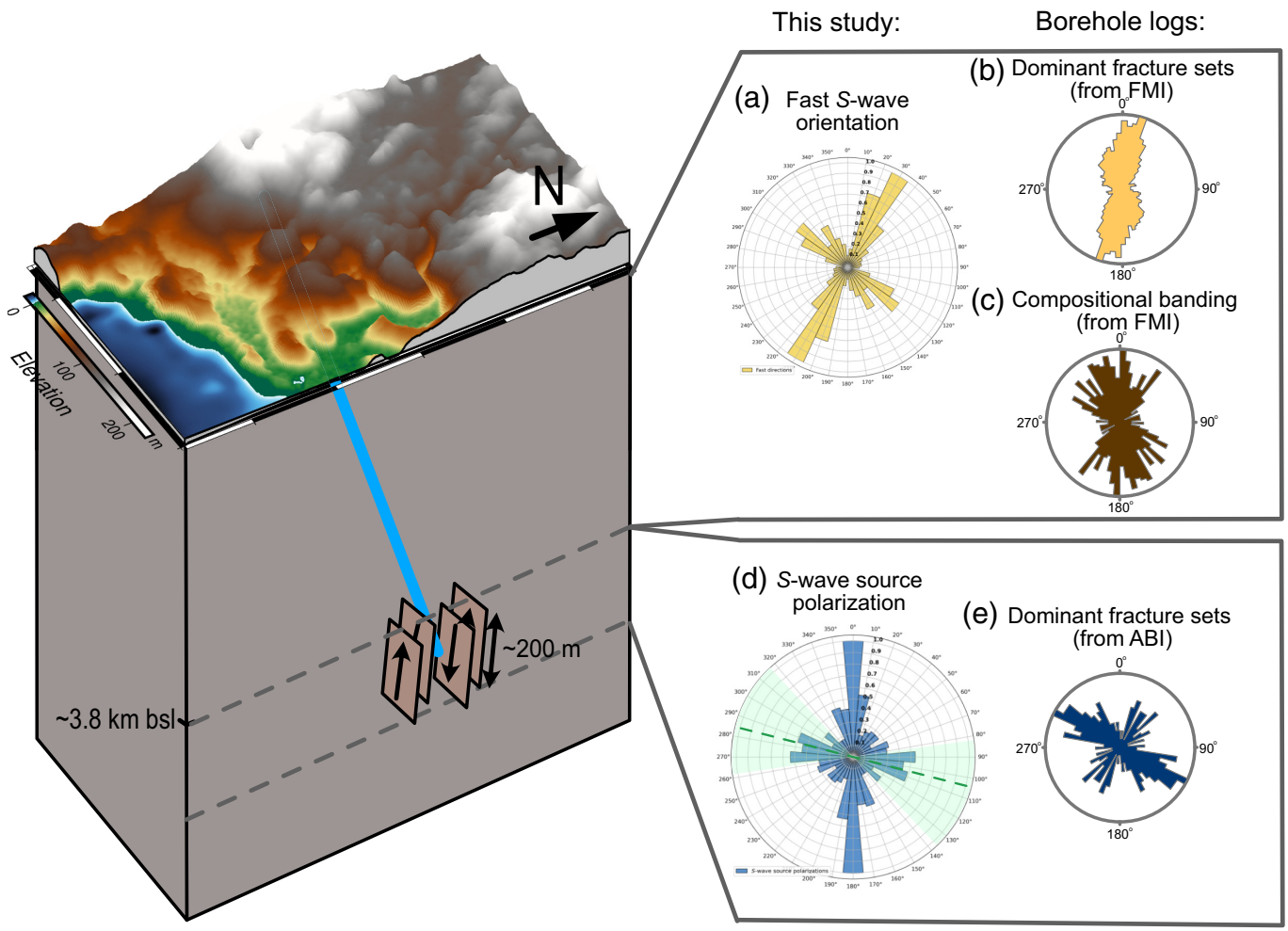

seismicity with well-log inferred fracture zones, constrain moment tensor inversions, and measure crustal anisotropy. All the procedures are fully automated, essential for processing such large nodal datasets. This is deliberate, emphasizing the consistency of results and the benefits of high data volumes for reducing the influence of spurious observations.

Tomographic imaging, particularly velocity structure, would further improve the constraint of earthquake hypocenters when also potentially mapping subsurface fluid migration and accumulation. However, we do not perform tomography here because a single cluster of seismicity around the injection region does not provide adequate constraint of body-wave tomographic inversion. It may be possible for double-difference tomography to constrain velocity structure within the injection region (Zhang and Thurber, 2006), and surface-wave tomography could provide insight into overall crustal velocity structure. Given the proximity to the coast, ambient noise sources may provide the most promise for probing the subsurface, although the limited frequency response below 1 Hz will limit resolution with increasing depth. Overall, however, the greatest limitations of nodes are battery life and no real-time telemetry, limiting their application for real-time, long-term monitoring.

We envisage that nodes will play an important role in geothermal system development. Going forward, it is feasible to

Figure 5. Summary of insights into the geothermal system provided by the node deployment and a comparison to borehole log data from well EG-1 (provided by Eden Geothermal Ltd). The blue line on the left schematic is the approximate well trajectory. (a) Fast *S*-wave orientations from this study. (b,c) Dominant fracture sets and compositional banding from formation microresistivity imaging (FMI)-derived well-log interpretations, respectively, from 1500 to 3900 m depth below the surface. (d) *S*-wave source polarizations and nodal plane orientations from this study. (e) Dominant fracture sets from acoustic micro imaging (AMI)-derived well-log interpretations from 3800 to 4100 m depth below the surface. The injection zone is at ~3500–4300 m depth below the surface.

deploy tens of thousands of nodes with network apertures of the order of 10 km. Given the typical source–receiver geometry limitations of surface deployments with single clusters of seismicity, we suggest that where possible, DAS technology is deployed at least downhole (Lellouch *et al.*, 2020; Verdon *et al.*, 2020) to increase the ray path coverage for source inversion and tomography. Overall, although current battery life and lack of telemetry limit nodes for long-term monitoring, the technology shows much promise for enhancing network coverage during critical periods of geothermal reservoir development, such as stimulation.

Data and Resources

Continuous seismograms and well logs analyzed in this study are proprietary, with conventional seismometer and well-log data provided by Eden Geothermal Ltd. However, analyzed data used to plot the results presented here are archived in a permanent Zenodo repository (doi: 10.5281/zenodo.10677930). The supplemental material is included to provide additional notes on the deployment, data processing parameters, instrument performance and additional results in more detail. This information is included to help aid reproducibility and inform readers on the limitations of the analysis.

Declaration of Competing Interests

The seismic instrumentation for this experiment was provided by STRYDE Ltd. Logistical support and auxiliary data were provided by Eden Geothermal Ltd. However, although the authors are grateful and acknowledge this support, academic independence was retained throughout, with authors from the aforementioned organizations only included where they provided an unbiased, scientific contribution. The authors acknowledge that there are no conflicts of interest recorded.

Acknowledgments

The authors thank Eden Geothermal Ltd for all their support, including data-sharing and providing logistical support for the seismic deployment. The authors particularly appreciate the support of Claire Judd and Steve Mabbot. The authors also thank Roy Baria for insightful discussions. The authors thank the many landowners who welcomed us onto their land to deploy nodes. There are too many to name individually here, but we are truly grateful for their support, without which this work would not have been possible. The authors also thank STRYDE Ltd for loaning us the nodes for the deployment and for their subsequent technical expertise and guidance, especially regarding the preprocessing of the data. Finally, the authors thank two anonymous reviewers and the editor for comments that no doubt improved the article. This project was partially supported via the Natural Environment Research Council UKUH Challenge grant project SHAPE-UK (Grant Number NE/R018006/1). T. Hudson was supported by a Leverhulme Early Career Fellowship (ECF-2022-499). T. Kettlety was funded by a fellowship from Oxford Net Zero, a Strategic Research Fund project of the University of Oxford, and also by Linacre College. R. K. Shail was supported in earlier work with Eden Geothermal by the European Regional Development Fund/United Kingdom Government.

References

Arnold, R., and J. Townend (2007). A Bayesian approach to estimating tectonic stress from seismological data, *Geophys. J. Int.* **170,** no. 1, 1336–1356, doi: 10.1111/j.1365-246X.2007.03485.x.

Baria, R., A. S. P. Green, and R. H. Jones (1989). Anomalous seismic events observed at the CSM HDR project, U.K., *Int. J. Rock Mech. Min. Sci.* **26,** nos. 3/4, 257–269, doi: 10.1016/0148-9062(89)91975-X.

Booth, D. C. (2010). UK 1-D regional velocity models by analysis of variance of *P*-wave travel times from local earthquakes, *J. Seismol.* **14,** no. 2, 197–207, doi: 10.1007/s10950-009-9160-4.

Brune, J. N. (1970). Tectonic stress and the spectra of seismic shear waves from earthquakes, *J. Geophys. Res.* **75,** no. 26, 4997–5009.

Clarke, H., J. P. Verdon, T. Kettlety, A. F. Baird, and J. M. Kendall (2019). Real-time imaging, forecasting, and management of human-induced seismicity at Preston new road, Lancashire, England, *Seismol. Res. Lett.* **90,** no. 5, 1902–1915, doi: 10.1785/0220190110.

Edwards, B., T. Kraft, C. Cauzzi, P. Kästli, and S. Wiemer (2015). Seismic monitoring and analysis of deep geothermal projects in St. Gallen and Basel, Switzerland, *Geophys. J. Int.* **201,** no. 2, 1022–1039, doi: 10.1093/gji/ggv059.

Gauntlett, M., T. Hudson, J. M. Kendall, N. Rawlinson, J. Blundy, S. Lapins, B. Goitom, J. Hammond, C. Oppenheimer, and G. Ogubazghi (2023). Seismic tomography of Nabro Caldera, Eritrea: Insights into the magmatic and hydrothermal systems of a recently erupted volcano, *J. Geophys. Res.* **128,** no. 5, 1–21, doi: 10.1029/2022JB025742.

Goertz-Allmann, B. P., and S. Wiemer (2012). Geomechanical modeling of induced seismicity source parameters and implications for seismic hazard assessment, *Geophysics* **78,** no. 1, KS25–KS39, doi: 10.1190/GEO2012-0102.1.

Grigoli, F., S. Cesca, E. Priolo, A. P. Rinaldi, J. F. Clinton, T. A. Stabile, B. Dost, M. G. Fernandez, S. Wiemer, and T. Dahm (2017). Current challenges in monitoring, discrimination, and management of induced seismicity related to underground industrial activities: A European perspective, *Rev. Geophys.* **55,** no. 2, 310–340, doi: 10.1002/2016RG000542.

Holmgren, J. M., and M. J. Werner (2021). Raspberry shake instruments provide initial ground-motion assessment of the induced

seismicity at the United downs deep geothermal power project in Cornwall, United Kingdom, *Seism. Rec.* **1,** no. 1, 27–34, doi: 10.1785/0320210010.

Hudson, T. S., J. Asplet, and A. M. Walker (2023). Automated shear-wave splitting analysis for single- and multi-layer anisotropic media, *Seismica* **2,** no. 2, doi: 10.26443/seismica.v2i2.1031.

Hudson, T. S., J. M. Kendall, J. D. Blundy, M. E. Pritchard, P. MacQueen, S. S. Wei, J. H. Gottsmann, and S. Lapins (2023). Hydrothermal fluids and where to find them: Using seismic attenuation and anisotropy to map fluids beneath Uturuncu volcano, Bolivia, *Geophys. Res. Lett.* **50,** no. 5, 1–16, doi: 10.1029/2022GL100974.

Hudson, T. S., J. M. Kendall, M. E. Pritchard, J. D. Blundy, and J. H. Gottsmann (2022). From slab to surface: Earthquake evidence for fluid migration at Uturuncu volcano, Bolivia, *Earth Planet. Sci. Lett.* **577,** 117268, doi: 10.1016/j.epsl.2021.117268.

Hudson, T. S., J. Smith, A. M. Brisbourne, and R. S. White (2019). Automated detection of basal icequakes and discrimination from surface crevassing, *Ann. Glaciol.* **60,** no. 79, 167–181, doi: 10.1017/aog.2019.18.

Igonin, N., J. P. Verdon, J. M. Kendall, and D. W. Eaton (2021). Large-scale fracture systems are permeable pathways for fault activation during hydraulic fracturing, *J. Geophys. Res.* **126,** no. 1, 1–19, doi: 10.1029/2020JB020311.

Kendall, J. M. (2000). Seismic anisotropy in the boundary layers of the mantle, in *Earth's Deep Interior: Mineral Physics and Tomography from the Atomic to the Global Scale*, S.-I. Karato, A. Forte, R. Liebermann, G. Masters, and L. Stixrude (Editors), Vol. 117, Geophysical Monograph Series, American Geophysical Union, Washington, D.C., 133–159, doi: 10.1029/GM117p0133.

Kettlety, T., J. P. Verdon, A. Butcher, M. Hampson, and L. Craddock (2021). High-resolution imaging of the M_L 2.9 August 2019 earthquake in Lancashire, United Kingdom, induced by hydraulic fracturing during Preston new road PNR-2 operations, *Seismol. Res. Lett.* **92,** no. 1, 151–169, doi: 10.1785/0220200187.

Kingdon, A., J. Williams, M. Fellgett, N. Rettelbach, and O. Heidbach (2022). Stress Map of Great Britain and Ireland 2022, *GFZ German Research Center for Geosciences*, doi: 10.5880/WSM.GreatBritainIreland2022.

Lellouch, A., R. Schultz, N. J. Lindsey, B. L. Biondi, and W. L. Ellsworth (2020). Low-magnitude seismicity with a downhole distributed acoustic sensing array—Examples from the FORGE geothermal experiment, *J. Geophys. Res.* **126,** no. 1, doi: 10.1029/2020jb020462.

Lomax, A., and J. Virieux (2000). Probabilistic earthquake location in 3D and layered models, in *Advances in Seismic Event Location*, C. H. Thurber and N. Rabinowitz (Editors), Vol. 18, Series Modern Approaches in Geophysics, Springer, Dordrecht,101–134.

Madariaga, R. (1976). Dynamics of an expanding circular fault, *Bull. Seismol. Soc. Am.* **66,** no. 1, 639–666.

McKenzie, D. P. (1969). The relation between fault plane solutions for earthquakes and the directions of the principal stresses, *Bull. Seismol. Soc. Am.* **59,** no. 2, 591–601.

Napolitano, F., L. De Siena, A. Gervasi, I. Guerra, R. Scarpa, and M. La Rocca (2020). Scattering and absorption imaging of a highly fractured fluid-filled seismogenetic volume in a region of slow deformation, *Geosci. Front.* **11,** no. 1, 989–998, doi: 10.1016/j.gsf.2019.09.014.

Obermann, A., P. Sánchez-Pastor, S. Wu, C. Wollin, A. F. Baird, M. P. Isken, J. Clinton, B. P. AllmannGoertz-, T. Dahm, A. Wuestefeld, *et al.* (2022). Combined large- N seismic arrays and DAS fiber optic cables across the Hengill Geothermal Field, Iceland, *Seismol. Res. Lett.* **93,** no. 5, 2498–2514, doi: 10.1785/0220220073.

Ourabah, A., and A. Chatenay (2022). Unlocking ultra-high-density seismic for CCUS applications by combining nimble nodes and agile source technologies, *Lead. Edge* **41,** no. 1, 27–33, doi: 10.1190/tle41010027.1.

Ourabah, A., L. Petronio, A. Affatato, L. Baradello, N. Goujon, and Z. Song (2021). Using 1C nodes in a 3C combination—Benefits, and inconveniences, *NSG2021 27th European Meeting of Environmental and Engineering Geophysics*, European Association of Geoscientists and Engineers, 1–5, doi: 10.3997/2214-4609.202120139.

Parker, L. M., C. H. Thurber, X. Zeng, P. Li, N. E. Lord, D. Fratta, H. F. Wang, M. C. Robertson, A. M. Thomas, M. S. Karplus, *et al.* (2018). Active-source seismic tomography at the brady geothermal field, Nevada, with dense nodal and fiber-optic seismic arrays, *Seismol. Res. Lett.* **89,** no. 5, 1629–1640, doi: 10.1785/0220180085.

Pugh, D. J., and R. S. White (2018). MTfit: A Bayesian approach to seismic moment-tensor inversion, *Seismol. Res. Lett.* doi: 10.1785/0220170273.

Pugh, D. J., R. S. White, and P. A. F. Christie (2016). Automatic Bayesian polarity determination, *Geophys. J. Int.* **206,** no. 1, 275–291, doi: 10.1093/gji/ggw146.

Savage, M. K., Y. Aoki, K. Unglert, T. Ohkura, K. Umakoshi, H. Shimizu, M. Iguchi, T. Tameguri, T. Ohminato, and J. Mori (2016). Stress, strain rate and anisotropy in Kyushu, Japan, *Earth Planet. Sci. Lett.* **439,** 129–142, doi: 10.1016/j.epsl.2016.01.005.

Schoenball, M., L. Dorbath, E. Gaucher, J. F. Wellmann, and T. Kohl (2014). Change of stress regime during geothermal reservoir stimulation, *Geophys. Res. Lett.* **41,** no. 4, 1163–1170, doi: 10.1002/2013GL058514.

Sherburn, S., S. M. Sewell, S. Bourguignon, W. Cumming, S. Bannister, C. Bardsley, J. Winick, J. Quinao, and I. C. Wallis (2015). Microseismicity at Rotokawa geothermal field, New Zealand, 2008-2012, *Geothermics* **54,** 23–34, doi: 10.1016/j.geothermics.2014.11.001.

Trugman, D. T., and P. M. Shearer (2017). GrowClust: A hierarchical clustering algorithm for relative earthquake relocation, with application to the Spanish Springs and Sheldon, Nevada, earthquake sequences, *Seismol. Res. Lett.* **88,** no. 2, 379–391, doi: 10.1785/0220160188.

Verdon, J. P., S. A. Horne, A. Clarke, A. L. Stork, A. F. Baird, and J.-M. Kendall (2020). Microseismic monitoring using a fibre-optic distributed acoustic sensor (DAS) array, *Geophysics* **85,** no. 1, 1–48, doi: 10.1190/geo2019-0752.1.

Wuestefeld, A., O. Al-Harrasi, J. P. Verdon, J. Wookey, and J. M. Kendall (2010). A strategy for automated analysis of passive microseismic data to image seismic anisotropy and fracture

characteristics, *Geophys. Prospect.* **58,** no. 5, 755–773, doi: 10.1111/j.1365-2478.2010.00891.x.

Zang, A., V. Oye, P. Jousset, N. Deichmann, R. Gritto, A. McGarr, E. Majer, and D. Bruhn (2014). Analysis of induced seismicity in geothermal reservoirs—An overview, *Geothermics* **52,** 6–21, doi: 10.1016/j.geothermics.2014.06.005.

Zhang, H., and C. Thurber (2006). Development and applications of double-difference seismic tomography, *Pure Appl. Geophys.* **163,** nos. 2/3, 373–403, doi: 10.1007/s00024-005-0021-y.

Zhang, H., D. W. Eaton, G. Rodriguez, and S. Q. Jia (2019). Source-mechanism analysis and stress inversion for hydraulic-fracturing-induced event sequences near Fox Creek, Alberta, *Bull. Seismol. Soc. Am.* **109,** no. 2, 636–651, doi: 10.1785/0120180275.

Manuscript received 31 May 2024
Published online 22 July 2024